WATER RESOURCES RESEARCH, VOL. 30, NO. 9, PAGES 2533–2546, SEPTEMBER 1994

Gravity-driven infiltration instability in initially dry nonhorizontal fractures

M. J. Nicholl and R. J. Glass
Geoscience Center, Sandia National Laboratory, Albuquerque, New Mexico

S. W. Wheatcraft
Department of Geological Sciences, University of Nevada, Reno

Abstract. Experimental evidence demonstrating gravity-driven wetting front instability in an initially dry natural fracture is presented. An experimental approach is developed using a transparent analog rough-walled fracture to explore gravity-driven instability. Three different boundary conditions were observed to produce unstable fronts in the analog fracture: application of fluid at less than the imbibition capacity, inversion of a density-stratified system, and redistribution of flow at the cessation of stable infiltration. The redistribution boundary condition (analogous to the cessation of ponded infiltration) is considered in a series of systematic experiments. Gravitational gradient and magnitude of the fluid input were varied during experimentation. Qualitative observations imply that finger development is strongly correlated to the structure of the imbibition front at the onset of flow redistribution. Measurements of fingertip velocity are used to develop a first-order relationship with fingertip length. Measured finger width is compared to theoretical predictions based on linear stability theory.

Introduction

Development of appropriate conceptual models for flow through unsaturated fractured rock must be based on an adequate understanding of the many small-scale processes which govern flow within the system. Most current models assume fractures behave in a fashion similar to thin layers of porous media, with saturation/pressure relationships analogous to those of sand (see reviews by *Pruess and Wang* [1987], *Evans and Nicholson* [1987], and *Eaton et al.* [1990]). At macroscopic scales, such models yield flat infiltration fronts and uniform wetted structures within the fracture. However, the influence of gravity can cause infiltration flow instability in nonhorizontal fractures, leading to the formation of gravity-driven fingers and nonuniform wetted structures [*Nicholl et al.*, 1992]. These fingers form regardless of fluid imbibition into adjacent matrix blocks [*Glass and Tidwell*, 1991].

Instability of a dynamic system is defined as the unconstrained growth of the inevitably occurring small perturbations to the system. Competition between viscous and gravitational forces controls interface stability during fluid-fluid displacement. The contemporaneous works of *Saffman and Taylor* [1958] and *Chouke et al.* [1959] used first-order linear stability theory to consider the stability of fluid-fluid displacement in a porous media or Hele-Shaw cell. Results from both groups suggested that in addition to interfacial velocity (U), system stability was a function of differences in fluid viscosity (μ), fluid density (ρ), and effective permeability of the media to the relevant fluids (k). Following the somewhat less restrictive approach of *Chouke et al.* [1959], we consider a two-fluid system (subscripts 1 and 2) separated by a flat interface, with the coordinate system defined such that the upward directed Z axis is positive. Steady planar displacement was shown to be unstable for perturbations to the interface of all wavelengths when the following inequality is satisfied:

$$U\left\{\frac{\mu_2}{k_2}-\frac{\mu_1}{k_1}\right\}+(\rho_2-\rho_1)g\cos\alpha>0 \qquad (1)$$

where g is gravitational acceleration and α is the inclination from vertical of the interfacial normal directed from fluid 1 into fluid 2.

Viscous instability occurs when a more viscous fluid is displaced by a less viscous fluid and gravitational forces do not act to fully stabilize the interface. This phenomenon is of significant interest with respect to petroleum extraction and is amenable to controlled laboratory experimentation. Numerous theoretical and experimental studies of viscous instability in porous media and Hele-Shaw cells, which are physical analogs for saturated flow through porous media and smooth-walled fractures, are reported in the literature (see reviews by *Saffman* [1986] and *Homsy* [1987]).

Gravity-driven instability occurs when a dense fluid overlies a lighter fluid and viscous forces do not act to fully stabilize a displacement front. Equation (1) may be simplified for infiltration of water into a dry, air-filled Hele-Shaw cell or porous medium by neglecting the density and viscosity of air with respect to those of water. The resultant inequality (equation (2)) simply states that a downward moving infiltration front will be unstable when the flux (q) through the system is less than the gravitationally driven saturated flux given by the product of saturated conductivity (K_s) and gravitational gradient (G_g):

Paper number 94WR00164.
0043-1397/94/94WR-00164$05.00

$$q < K_s G_g \tag{2a}$$

where

$$K_s = k\rho g/\mu \tag{2b}$$

$$G_g = g \cos \alpha \tag{2c}$$

This instability is manifested as the break-up of a smooth front into discrete fingers oriented in the direction of G_g. Gravity-driven fingering is a different phenomenon than the heterogeneity-induced "channeling" that has been found in saturated natural fractures [e.g., *Neretnieks et al.*, 1982; *Neretnieks*, 1990]. It has been shown that under certain conditions, downward moving wetting fronts exhibit gravity-driven instability in unsaturated sands [e.g., *Hill and Parlange*, 1972; *White et al.*, 1976a; *Diment and Watson*, 1985; *Glass et al.*, 1989a, b, c; *Glass et al.*, 1991], smooth-walled Hele-Shaw cells [e.g., *White et al.*, 1976a, b; *Maxworthy*, 1987], and analog rough-walled fractures [*Nicholl et al.*, 1992].

Here we use experimentation to explore the formation of gravity-driven fingers during the infiltration of water into initially dry, nonhorizontal, rough-walled fractures. This experimentation considers a combination of instability mechanism, media geometry, fluid properties, and boundary conditions that has not previously been discussed in the literature. Research in Hele-Shaw cells, which are simply smooth-walled fractures, has been primarily directed toward understanding the viscosity-driven fingering associated with petroleum production (see review by *Homsy* [1987]). Work in rough-walled Hele-Shaw cells appears to be limited to the theoretical analysis of *de Gennes* [1986] which considers the impact on viscous instability of surface roughness on a scale that is much smaller than the mean aperture. The low viscosity and strong capillarity of water make it difficult to control boundary conditions such that a sharp transition between stable and unstable regimes is observed. As a result, water has historically been avoided as the driving fluid in Hele-Shaw experiments in favor of oil or glycerin.

To demonstrate that gravity-driven instability is a significant, real-world process, we begin by presenting an experiment performed in a natural fracture. Results of the natural fracture experiment lead to the development of an analog fracture created from rough-surfaced glass plates, thereby allowing wetting front dynamics to be studied in isolation from matrix interaction and macroscale aperture field heterogeneity. Digital imaging techniques were used to acquire detailed spatial and temporal data from the transparent analog fracture without influencing the system. Experiments demonstrating instability in the analog fracture under initially dry conditions are presented. Instability at the cessation of stable infiltration is considered in detail. A general description of flow field development is presented along with measurements of finger behavior obtained through systematic experimentation. First-order theory explaining the behavior of fingertip velocity is presented. Measured finger width is used to evaluate the applicability of linear stability theory to the finite amplitude perturbations considered in this study. Finally, we conclude by presenting a hypothetical field scenario, summarizing experimental results, and discussing potential research questions raised by this work.

Observed Finger Development in a Natural Fracture

A natural fracture sample was collected from the Bandelier Tuff, along State Route 4, near Los Alamos, New Mexico. The sample consisted of densely welded, gray, fine-grained rhyolite tuff, exhibiting small phenocrysts of quartz and sanidine. Surface area of the near planar fracture was approximately 2200 cm^2. Mating surfaces were carefully cleaned to remove debris and then reassembled in their original alignment. A clamping fixture was used to hold the fracture surfaces in close contact and orient the fracture along a vertical plane. The upper boundary of the sample fracture was oriented horizontally and surrounded with silicon putty to form a narrow reservoir; remaining boundaries were left open to atmospheric pressure. The effects of a single infiltration event in an initially dry fracture were simulated by rapidly flooding the reservoir with deionized water dyed blue with FD&C Blue No. 1 (1 g/L); approximately 0.4 cm^3/cm of fluid was applied per unit length of fracture.

At the conclusion of the experiment, the fracture was disassembled to allow examination of the wetted structure. Flow through the system was rapid with respect to matrix imbibition; as a result, smearing of the wetted structure due to matrix effects was minimal. The wetted region of the fracture (Plate 1) showed a distinct change in structure at approximately the 20-cm depth. The infiltrating front uniformly wetted the upper section of the fracture, implying a stable flow regime. Below the uniformly wetted zone, flow continued in the form of fingers, oriented in the direction of G_g. If the dominant flow process was heterogeneity-induced channeling, one would expect to observe preferential flow into regions of high capillary gradient. However, the observed wetted regions showed only minor deviation from the vertical direction, implying that gravity-driven instability dominated formation of the wetted structure below the uniformly wetted zone.

This experiment serves to accentuate the problems involved with the use of natural fractures. In order to develop a thorough understanding of the basic flow process it is necessary to obtain measured data from systematically varied experiments in a controlled system. In natural fractures, damage to the fracture surfaces during handling and changes in matrix pressures between successive experiments prevents accurate replication. Furthermore, fractured rocks vary significantly from sample to sample in terms of matrix interaction, aperture structure, and differential surface wettability, thereby precluding systematic variation of the relevant parameters. The only information obtainable from this experiment was the final wetted structure; data on finger velocity, dynamic structure, and the transition to instability could not be obtained. We therefore developed an experimental approach to allow systematic exploration of gravity-driven fingering in a rough-walled, transparent analog fracture.

Experimental Approach

Parameters relevant to flow through an unsaturated fracture are listed as follows.

1. Fluid properties include surface tension, viscosity, density, and contact angle.

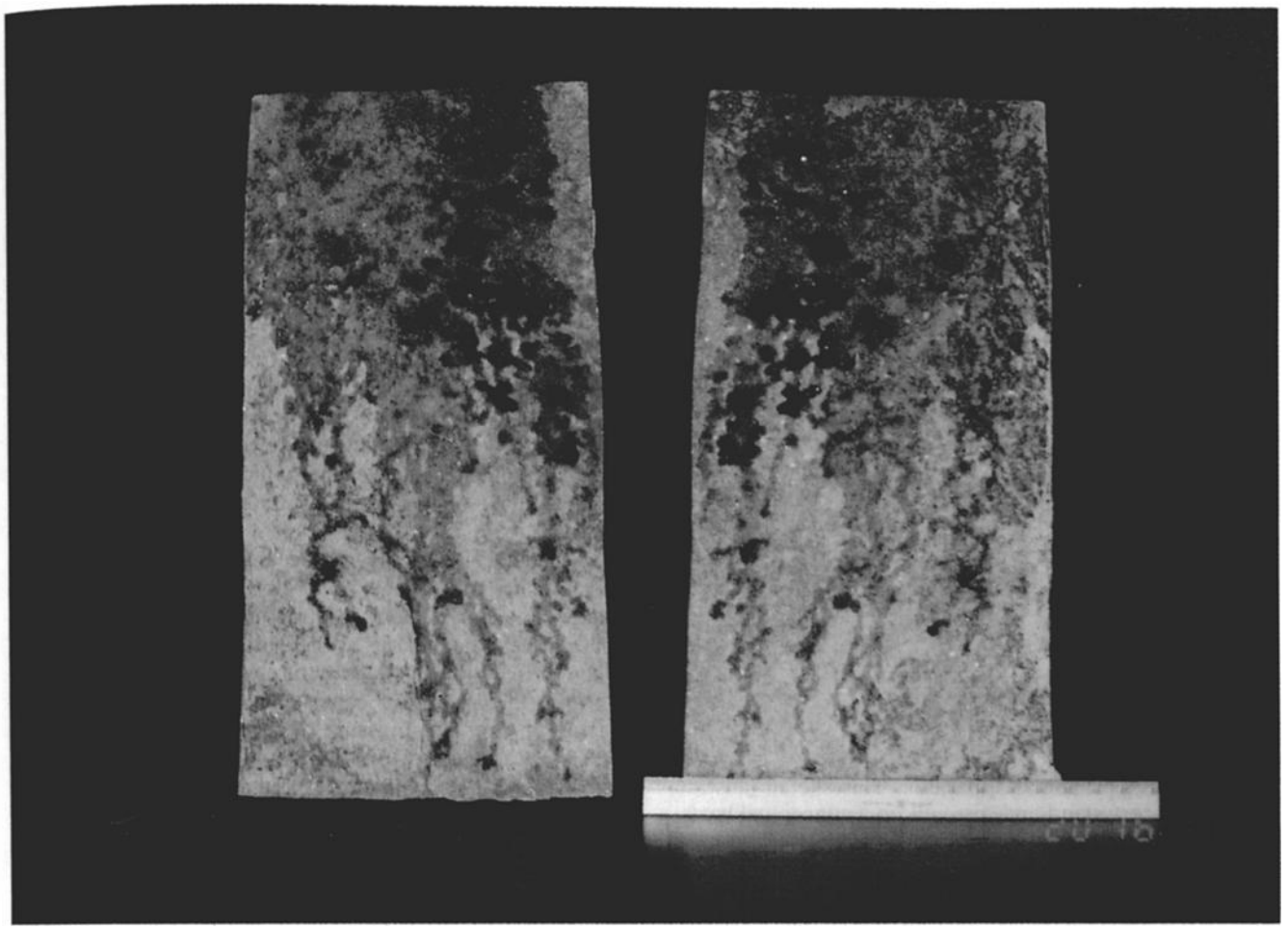

Plate 1. Wetting front instability in a natural fracture. The wetted structure implies that fluid advanced approximately 20 cm into the vertically oriented fracture as a stable front before breaking up into individual fingers. Path of the fingers shows that in this case, gravity-driven instability was the dominant process over heterogeneity-induced channeling.

2. Fracture properties include aperture distribution, spatial structure of aperture distribution, roughness length scales/microfracturing, and spatial variation of wettability.

3. Macroscopic fracture properties include geometric length scales and orientation relative to gravity.

4. Composite hydraulic properties include hydraulic conductivity, saturation/pressure relationship, and sorptivity.

5. Initial/boundary conditions include input flux, flow or no-flow fracture edge boundaries, initial saturation.

The parameters varied in this study were limited to gravitational gradient and magnitude of the fluid input. To develop a basic understanding of the flow process, experiments were conducted in the simplest possible rough-walled fracture; an analog assembled from two plates of commercially available "obscure" glass. This material is smooth on one side and has a formed texture on the other, with a nominal thickness of 0.48 cm. Placing the textured sides of two plates in close contact forms an analog aperture field. The mean aperture and hydraulic conductivity of the resultant statistically homogeneous aperture field falls within the realm characteristic of natural fractures. The impermeable surface of the plates eliminates matrix interaction. The test fracture may be disassembled for cleaning and reassembled in an repeatable alignment, thereby allowing replication of experiments under nearly identical conditions. Finally, the transparent nature of glass plates allows the use of digital imaging techniques to collect wetted structure data in a nonintrusive manner.

Experimental Apparatus

An experimental apparatus (Figure 1) composed of a rotating test stand, fracture test cell, and transmitted light visualization system was designed to facilitate observation of wetting front advance in transparent analog fractures. The test stand holds a test cell containing the analog fracture, digital camera, and lighting system in rigid, reproducible alignment. Test cells of up to 100 × 50 cm can be clamped onto the test plane table of the test stand. The analog fracture in the test cell is backlit by high-frequency fluorescent lamps built into a light box attached to the back side of the test plane table. Data are acquired by a charge-coupled device (CCD) video camera attached to the superstructure of the test stand and focused on the fracture plane. The test stand was designed such that the rigidly connected light box, test plane table, and camera could be rotated on the support base through more than 180 degrees, thereby allowing variation of G_g.

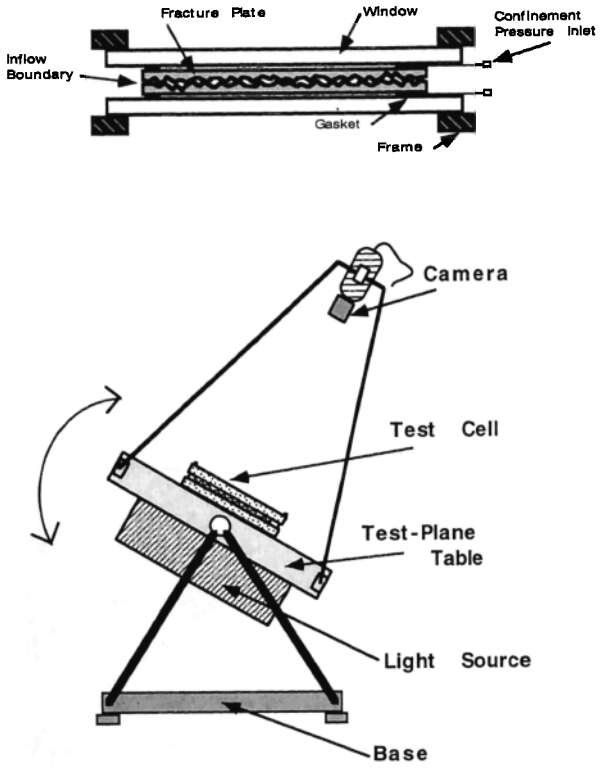

Figure 1. Experimental apparatus. This sketch illustrates the rotating test stand and test cell on a conceptual basis.

The test cell consists of two rectangular aluminum frames with 1.9-cm-thick plate glass windows (Figure 1). A 61 × 30.5 cm fracture plate is mounted to the inside of each plate glass window with a clear urethane gasket forming a pressure container between the window and test plate. The cell is assembled by placing the fracture plates in contact and bolting the aluminum frames together. Bolts are tightened using a six-stage crossing pattern to produce a uniform bolt torque of 8 inch-pounds (0.904 N m). Compressed air is used to pressurize each side of the fracture to 20 pounds per square inch (138 Pa), eliminating long-wavelength disturbances in the aperture field by forcing the fracture plates to be in close contact; fracture boundaries remain open to atmospheric pressure.

All experiments were digitally imaged and recorded at predetermined intervals. The PC-based image-acquisition system acquired data at 512 × 512 pixels, 256 gray levels/pixel resolution using a CCD camera. Pure deionized water provided insufficient contrast for the imaging system. Experimental fluid consisted of 1 g FD&C Blue No. 1 and 1 g FD&C Red No. 3 added to 1 L of deionized water, producing a deep blue-purple color. Wetting properties of the experimental fluid were evaluated using glass capillary tubes and were found to be consistent with that of deionized water.

Analog Fracture Characterization

When placed under a confining pressure, the formed-surface textures of the analog fracture create a statistically homogeneous aperture field. Contact area is negligible, as the texture of the plates does not produce perfectly mating surfaces and the rigid glass plates are subject to only minimal local deformation at contact points. Both horizontal imbibition and vertical drainage tests on the experimental fracture failed to indicate any significant heterogeneity away from the boundaries. *Glass* [1993a, b] presents a numerical model of the analog aperture field used in the experiments presented here. The topography of one surface from the analog fracture was measured at 0.1-mm resolution by laser profilometry over a 25.6 × 25.6 mm section. The aperture field was then numerically modeled by taking two identical profiles and fitting them in a manner that yielded the mean aperture of the experimental fracture as measured by volumetric imbibition. A gray scale image illustrating the structure of the model aperture field is shown as Figure 2a, along with the model aperture histogram (Figure 2b). Correlation length of the model aperture field was approximately 0.7 mm, much smaller than the narrowest finger observed. The homogeneous nature of the analog aperture field at the scale of interest eliminates heterogeneity-induced channeling as a possible cause of the observed preferential flow structures (fingers).

Saturated conductivity of the analog fracture was estimated using a test cell that allowed implementation of no-flow boundaries along the fracture sides (long axis) and constant head boundaries at the ends. Glass plates identical to those used in the analog fracture were sized to fit this cell (30.48 × 15.24 cm). For consistency with the experimental fracture, a confining pressure of 20 pounds per square inch (138 Pa) was applied. Sixty-eight experimental trials were performed. Assuming that measured mean aperture provides an appropriate characteristic length of the analog fracture, K_s was found to be constant for Reynolds numbers between 0.27 and 5.93, exhibiting a mean value of 3.13 cm/s and a standard deviation of 0.11. The parallel plate approximation yields a hydraulic aperture of 0.196 mm (standard deviation, 0.004). The measured mean aperture ($\hat{a}$) was somewhat smaller than that of the analog fracture used in the experiments (0.213 versus 0.225 mm). Assuming that K_s varies as

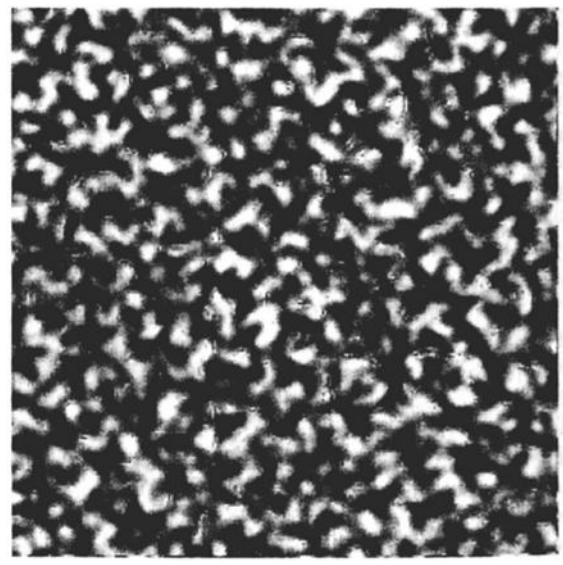

Figure 2a. Simulated aperture field. Gray scale image illustrates the model aperture structure; black indicates the smallest apertures and white indicates the largest. Field is 256 × 256 points over an area of 2.56 cm × 2.56 cm (taken from *Glass* [1993a, b]).

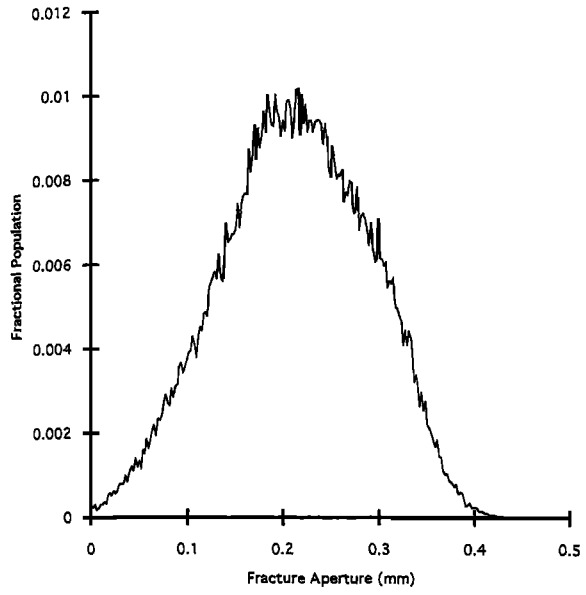

Figure 2b. Histogram of the model aperture field (taken from *Glass* [1993a, b]).

the square of the mean aperture (parallel plate approximation) leads to an estimate of K_s for the experimental analog fracture of 3.48 cm/s (standard deviation, 0.12).

Few comparable measurements of natural fractures are reported in the literature. Many reported measurements are based on in situ hydraulic tests and may not be reliable due to tenuous assumptions regarding fracture extent and connectivity [*Bourke et al.*, 1985]. The most appropriate measurements for comparison are probably those of *Hakami* [1989] on epoxy replicas of natural fractures in leptite, quartz-monzonite, and granite. Mean apertures were reported over a range from 0.084 to 0.462 mm (standard deviation, 0.046 to 0.449) with K_s values that ranged from 1.14 to 14.0 cm/s. Measurements from our analog fracture fall comfortably within these ranges. Two-dimensional measurements of mean aperture collected from the Pikes Peak granite showed a range of 0.12–5.41 mm [*Snow*, 1970]; our analog fracture falls near the low end of these reported aperture measurements.

Full Field Instability Experiments: Initially Dry Analog Fracture

By analogy to porous media and Hele-Shaw cell studies, it is expected that uniform application of fluid to an inclined, initially dry fracture at less than the gravitationally driven saturated flux (K_sG_g) will result in an unstable wetting front. In preliminary trials, this boundary condition was implemented by using a porous plate and positive-displacement pump to provide a distributed source along the upper boundary of a vertical fracture. Absorbent toweling was sandwiched between the fracture and the porous plate to assure hydraulic contact. Fingers initiated at the inflow boundary, apparently in response to local heterogeneity. Point connections associated with local heterogeneity created preferential flow paths. The resultant finite perturbations to the wetting front immediately developed into fingers in this unstable system. A similar instability mechanism in layered sands was reported by *Glass et al.* [1988]. The abrupt onset of fingering in the fracture prohibited investigation or control of the transition from stable to unstable flow. As this boundary condition merely requires that an initially dry fracture receive a steady supply of fluid at less than K_sG_g, there are numerous potential scenarios where it may occur in nature, including, but not limited to steady leakage from a low permeability unit, change in permeability along the fracture plane, and internal seepage resulting from a structural confluence.

A second situation known to exhibit gravity-driven instability in smooth-walled Hele-Shaw cells occurs when a dense fluid rests on top of a lighter one. This boundary condition is typically generated by "instantaneous" rotation of a stable cell in which the dense fluid is initially on the bottom [e.g., *Maxworthy*, 1987]. We explored this boundary condition by saturating a portion of the analog fracture by capillary imbibition from the lower boundary, yielding a macroscopically flat interface overlain by small perturbations associated with local heterogeneity. The test stand was then rapidly rotated such that the analog fracture was oriented vertically, with the experimental fluid along the upper boundary. Instability developed during rotation of the system, with fingers initiating from the most significant initial perturbations. This experiment is typically performed in smooth-walled Hele-Shaw cells using viscous liquids so that the inversion is "instantaneous" with respect to interface velocity. While these experiments served to reinforce analogies between smooth and rough-walled Hele-Shaw cells, the boundary condition could not be implemented instantaneously in this air/water system and the methodology was discontinued. Finally, with regard to the relevance of this particular boundary condition, the authors feel that should an in situ natural fracture undergo such an inversion, wetting front instability would be the least interesting of the associated phenomena.

The remainder of this paper considers the expected instability associated with redistribution of flow following the cessation of stable infiltration, as was observed in the natural fracture experiments previously discussed. In the analog system, a stable infiltration front was produced by simultaneously injecting the contents of 16 evenly spaced syringes along the upper boundary of the fracture. A reservoir enclosing the fracture boundary allowed ponding of excess fluid when input rate exceeded the imbibition capacity of the fracture. This procedure yields initial/boundary conditions analogous to the surface ponding associated with a sudden precipitation event in an arid region. Application of a finite slug allows visualization of the stable infiltration front and subsequent transition to instability. Distributing the slug through multiple point sources induces long wavelength perturbations in the advancing front (Figure 3a). Differential application of fluid allows variation in the magnitude and spatial distribution of finite perturbations to the front.

A series of slug imbibition/redistribution experiments were conducted in the analog fracture under dry initial conditions (Table 1). Parameters varied during this series of experiments were limited to G_g and the amount of fluid applied to the fracture, expressed as the depth of fluid applied (L_i). Gravitational gradient was varied by positioning the test stand such that the fracture was inclined from vertical at angles of 0, 41.5, 60, and 75.5 degrees, corresponding to G_g of 1.0, 0.75, 0.50, and 0.25. L_i is defined as the average volume of fluid applied per unit cross-sectional

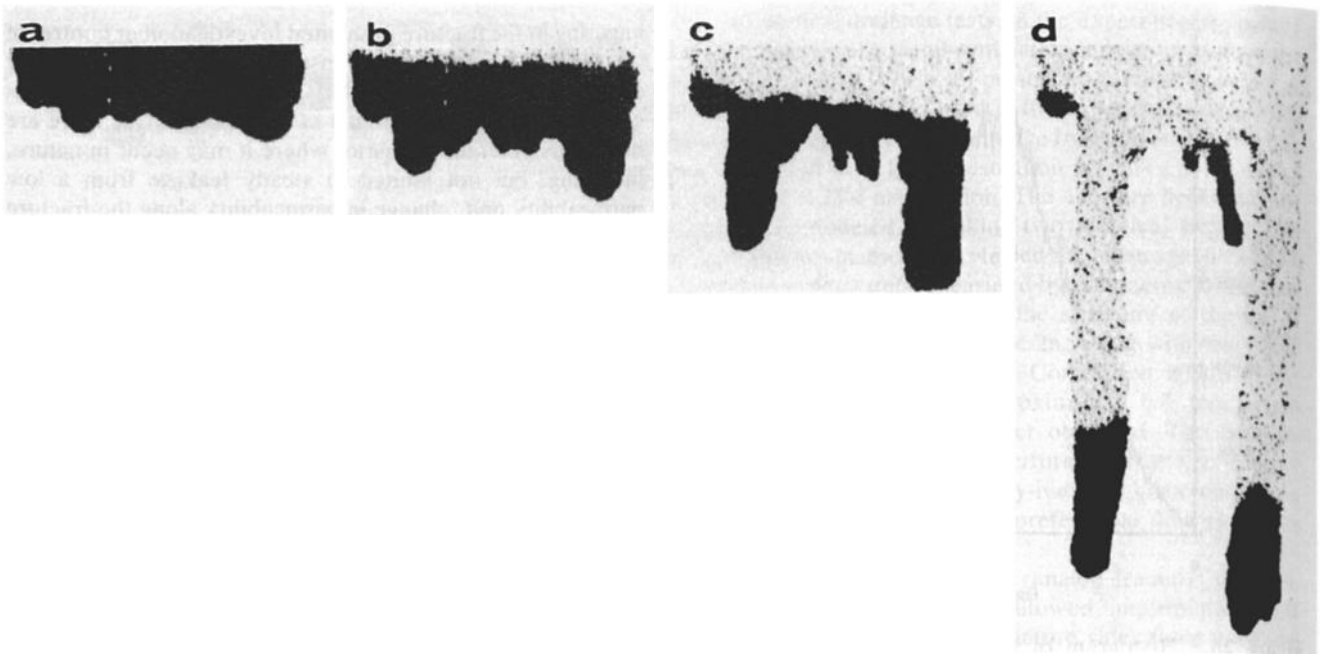

Figure 3. Sequence illustrating the development of instability in an initially dry fracture (experiment 8, $G_g = 0.75$, $L_i = 9.43$ cm); elapsed time (t) is defined as the interval between initial application of fluid and acquisition of the image. (a) Advancement of stable front ($t = 4$ s). (b) Onset of instability; note drainage along upper boundary ($t = 7$ s). (c) Development of fingers ($t = 13$ s). (d) Outside fingers fully developed, central finger starved of fluid ($t = 39$ s).

area of the fracture (fracture width multiplied by $\hat{a}$). Capillary properties and scale of the analog fracture limited variation of L_i to a range between approximately 5.4 and 37.9 cm. Fluid was applied with the intent of minimizing perturbations but without attempting to form a completely flat front. At the conclusion of each experiment, the analog fracture was disassembled and cleaned.

Results and Discussion

In this study, fingers were defined as structural features of the wetting front developing after the onset of redistribution, which are narrower than the initial stable front and show significant movement in the downgradient direction. The leading edge of such features consists of a coherent body of fluid fully spanning the fracture aperture. This leading edge will be referred to as the fingertip. Quantitative measurements of finger behavior including fingertip velocity, fingertip length, and finger width were obtained from the digital images; raw data are summarized in Table 1.

Mechanism for Instability

Total potential gradient (G_t) within the wetting front associated with slug infiltration is the resultant of two sets of forces: gravitational forces acting on the fluid body as a whole and capillary forces acting along the wetting and drying fronts,

$$G_t = G_g + G_c \tag{3}$$

Water entry pressure head (ψ_w) acts as a driving force, pulling the wetting front forward, while air entry pressure head (ψ_a) along the drying front acts to restrain movement. Following convention, ψ_w and ψ_a are defined as negative quantities such that abs (ψ_a) > abs (ψ_w). The coordinate system is defined such that the upward directed Z axis is positive (G_g is positive). If L_f is taken to be the length of the connected fluid column of spanned apertures measured parallel to G_g, the gradient due to capillary forces (G_c) may be approximated by

$$G_c \approx \frac{\psi_a - \psi_w}{L_f} \tag{4}$$

During ponded infiltration, no drainage occurs within the fracture; therefore the effects of a drying front should not be included in (4) ($\psi_a = 0$). The capillary gradient acts to reinforce flow ($G_c > 0$), and the downward gradient will be strongest at those points closest to the imbibition boundary. As a result, the gradient field during ponded infiltration causes perturbations to decrease in magnitude, which is a characteristic of system stability. When the ponded fluid is exhausted, drainage must occur within the fracture in order for the front to continue advancing. This creation of a drying front introduces ψ_a to (4), causing the capillary gradient to become negative and oppose G_g. At the onset of drainage, the horizontal upper boundary of the fracture creates a relatively flat drying front (Figure 3b). Hence the force opposing flow (G_c) is smallest at those points along the wetting front located furthest downgradient, causing a redistribution of flow to these locations and the growth of fingers.

General Description of Flow Field Structure

An illustrative example of the transition to instability and subsequent development of fingers is shown as Figure 3. The initial wetting front begins from 16 separate points that rapidly coalesce into a single front that is stable, but not flat (Figure 3a). Macroscopic features are caused by irregularities in the injection process, while smaller features result

Table 1. Summary of Experimental Data

Experiment Number	G_g	L_t, cm	Total Number of Fingers	Fingers Measured	V_{ave}, cm/s	W_{ave}, cm
25	1.00	6.25	5	3	1.53	2.70
13	1.00	8.99	4	2	2.37	5.37
23	1.00	14.91	1	0	I*	3.83†
16	1.00	20.49	2	0	3.07†	10.11†
24	1.00	24.26	2	0	I*	11.80†
26	1.00	28.40	1	1	3.12	23.46
27	1.00	34.00	1	1	3.31	26.82
22	0.75	5.68	2	2	1.01	3.34
8	0.75	9.43	2	2	1.29	5.51
19	0.75	9.98	4	2	0.97	2.85
4	0.75	10.23	3	3	1.27	3.87
17	0.75	10.26	5	2	0.99	3.14
20	0.75	13.67	2	2	1.73	6.74
10	0.75	18.68	2	2	2.03	7.95
21	0.75	24.38	1	0	I*	23.13†
11	0.75	28.17	2	0	I*	11.92†
18	0.75	33.15	1	0	I*	20.46†
12	0.75	33.47	1	1	2.33	26.03
44	0.75	37.95	1	0	I*	WF‡
28	0.50	5.39	1	1	0.49	4.52
7	0.50	8.89	3	3	0.70	3.41
2	0.50	9.85	2	2	0.71	4.52
29	0.50	14.40	1	1	1.17	10.40
50	0.50	14.59	2	2	0.92	6.49
51	0.50	15.93	2	2	0.75	6.24
30	0.50	19.38	3	3	0.91	5.82
31	0.50	21.84	2	1	1.04	6.98
49	0.50	28.75	1	0	1.20†	18.31†
1	0.50	WM§	2	0	1.04†	5.12†
6	0.25	9.08	1	1	0.30	4.50
45	0.25	14.41	1	1	0.30	5.99
46	0.25	19.21	1	0	0.31†	7.33†
47	0.25	23.75	2	2	0.28	7.56
48	0.25	28.91	2	0	0.28†	7.93†
43	0.25	33.37	2	2	0.32	6.97

Fifty-one experiments were performed. Experiments 5, 9, and 32 through 42 were invalidated due to operator error in the assembly process. Experiments 3, 14, and 15 were scoping experiments utilizing other boundary and initial conditions. Measurements were taken from significant, disconnected fingers. Individual absences of data are explained below.

*Boundary effects invalidated velocity measurements.

†Fingers did not disconnect; this datum was not used for analysis and is shown simply for completeness.

‡Extremely wide finger contacted the boundaries of the analog fracture.

§Improper measurement of sample weight invalidated this calculation.

from local heterogeneity in the aperture field. While fluid is entering the fracture from the reservoir, the magnitude of the macroscopic perturbations is observed to decrease; this dampening implies stability. Behavior of the wetting front changes entirely when the input slug is exhausted and redistribution begins. The pressure gradient quickly reverses to oppose fluid advancement within the fracture, velocity drops such that flux is no longer sufficient to support a stable wetting front ($q < K_s G_g$), and the onset of instability is observed (Figure 3b). The finite perturbations induced during the injection process now begin to grow, forming distinct fingers. The wavelength associated with this growth is of the same order as that associated with the stable, perturbed front at the onset of redistribution.

After the onset of instability, individual fingers rapidly develop (Figure 3c). The largest and fastest fingers consume the bulk of the available fluid. As a result, less robust fingers become disconnected from the fluid source, and hence are retarded (Figure 3d). The front shown in Figure 3b exhibits three growing fingers that have developed from spatial perturbations in the stable front. The center finger has the smallest L_f of the three fingers; as the force opposing flow (G_c) is inversely proportional to L_f, the gradient field induces preferential flow into the outer fingers, eventually starving the center finger (Figure 3d). Widely separated fingers are more likely to fully develop than ones located close together, as there is less competition for available fluid.

Drainage behind the advancing fingertips leaves a partially drained zone, wetted to "field capacity" of the fracture. Due to variation in the aperture field, saturation within the drained region exhibits a high degree of spatial variation. Disconnected clusters of fluid fully spanning the fracture aperture are seen as dark regions in Figures 3c and 3d. Because the fingertip is not replenished by flow through the drained region, it decreases in size with distance traveled. As L_f decreases, the force opposing flow (G_c) increases in

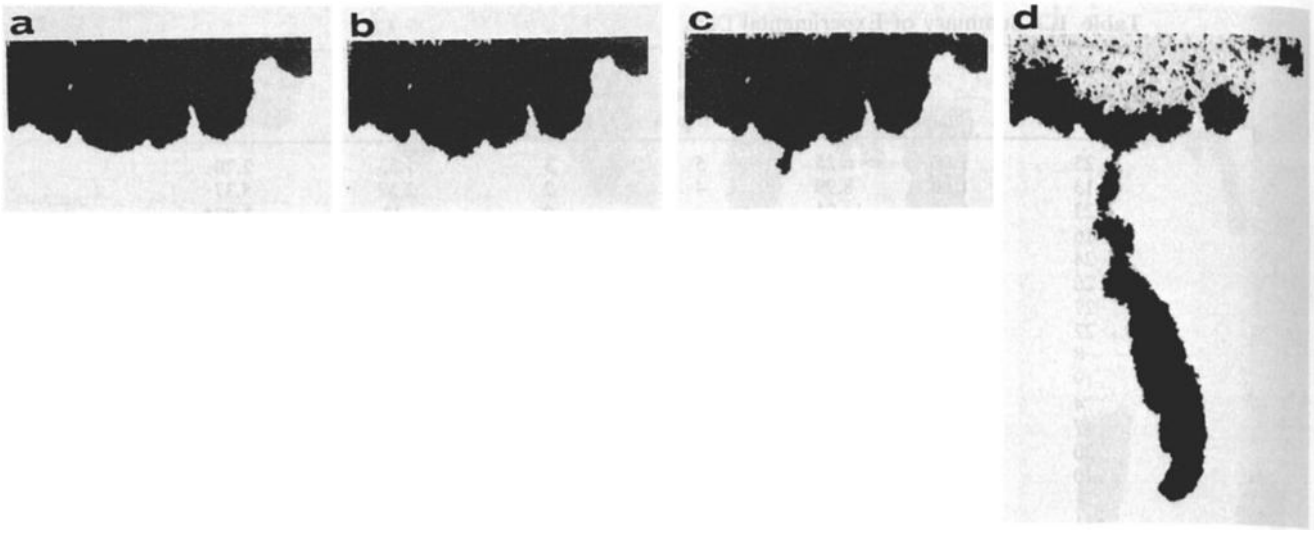

Figure 4. Percolation-type development of an unstable front, experiment 6 ($G_g = 0.25$, $L_i = 9.08$ cm. (a) Front is shown near the end of stable imbibition ($t = 39$ s). (b) Several minutes after the cessation of imbibition the front is nearly frozen in place, limited movement is occurring as local apertures are successively drained and spanned in a sequence of individual Haines jumps; note the small tendril forming on the largest perturbation ($t = 619$ s). (c) Movement continues on a discrete basis; however, the rate of drainage/filling is visibly increasing ($t = 1069$ s). (d) After L_s reaches a critical threshold, flow ceases to be on a discrete basis as observed at earlier times, leading to rapid formation of the finger shown ($t = 1518$ s).

magnitude, slowing the finger. When G_c is equal and opposite to G_g, the finger halts, becoming "frozen" in the fracture.

The spatial distribution of fingers was observed to be solely dependent on the magnitude and distribution of perturbations to the front at the onset of redistribution. Local heterogeneity within the fracture was observed to influence flow at a scale much smaller than that of individual fingers. The structure of the front results from damping of the initial perturbation waveform during stable imbibition. In general, short wavelengths are damped more rapidly than long. At large G_g, damping is reduced; therefore larger numbers of perturbations remain at the onset of instability. In the vertical experiments ($G_g = 1.0$) from 2 to 5 fingers were observed, at $G_g = 0.75$, 2–5 fingers, $G_g = 0.50$, 1–3 fingers, and at $G_g = 0.25$, 1–2 fingers. Increasing L_i increases the distance traveled by the stable front, and hence damping. At large L_i, perturbations to the front were of a sufficiently long wavelength that only one or two fingers could form in the 30.5-cm-wide test fracture.

Limits on Fluid Application

As previously stated, the depth of fluid applied (L_i) was varied between 5.4 and 37.9 cm. Fingers did not fully develop if L_i was much more than half the total length of the analog fracture (61 cm). The lower limit on L_i was governed by capillary forces. Equations (3) and (4) suggest that a sufficiently small quantity of fluid applied to an initially dry fracture will remain stationary within the fracture after the fluid reservoir is exhausted. For the fluid to move downward, gravitational and downward acting capillary forces must be sufficient to overcome the air entry pressure head required for drainage at the top boundary of the fracture. Movement is expected to initiate when

$$L_f G_g + (\psi_a - \psi_w) > 0 \qquad (5)$$

As L_f is correlated to L_i, small infiltration fronts are expected to penetrate a short distance into the fracture and then remain pinned in place by capillary forces. Experiment 6 ($L_i = 9.08$ cm, $G_g = 0.25$) exhibited borderline behavior; for several minutes after the onset of redistribution the front appeared to be frozen (Figures 4a and 4b). However, close examination revealed that the front was moving virtually "pore by pore" in the vicinity of maximum L_f, analogous to the process of invasion percolation modified to include gravitational effects [*Glass*, 1993a, b]. Approximately 24 min after injection a distinct tendril formed from the front, sharply increasing the local gradient (Figure 4c). The rate of pore filling was seen to increase very rapidly, forming the finger seen in Figure 4d. As the tendril lengthened into a finger, flow rate increased and finger width was observed to increase substantially.

Fingertip Velocity

As was discussed previously, independent variables were limited to gravitational gradient (G_g) and amount of fluid applied to the fracture, which is expressed as a length (L_i). Images illustrating how finger behavior is effected by increasing L_i and G_g are presented as Figures 5 and 6, respectively. The interval between initial application of fluid to the fracture and acquisition of the image, elapsed time (t), may be used to compare the effects of L_i and G_g on a qualitative basis. The experiment shown in Figure 5a advanced a shorter distance into the fracture in 32 s than the one shown in Figure 5d did in 23 s. The second front contains significantly more fluid (larger L_i) than the first, suggesting that finger velocity will exhibit a positive correlation with L_i; intermediate cases (Figures 5b and 5c) are consistent with this observation. The images shown in Figure 6 were selected such that finger advancement was comparable. The experiment shown in Figure 6a required 1518 s for the

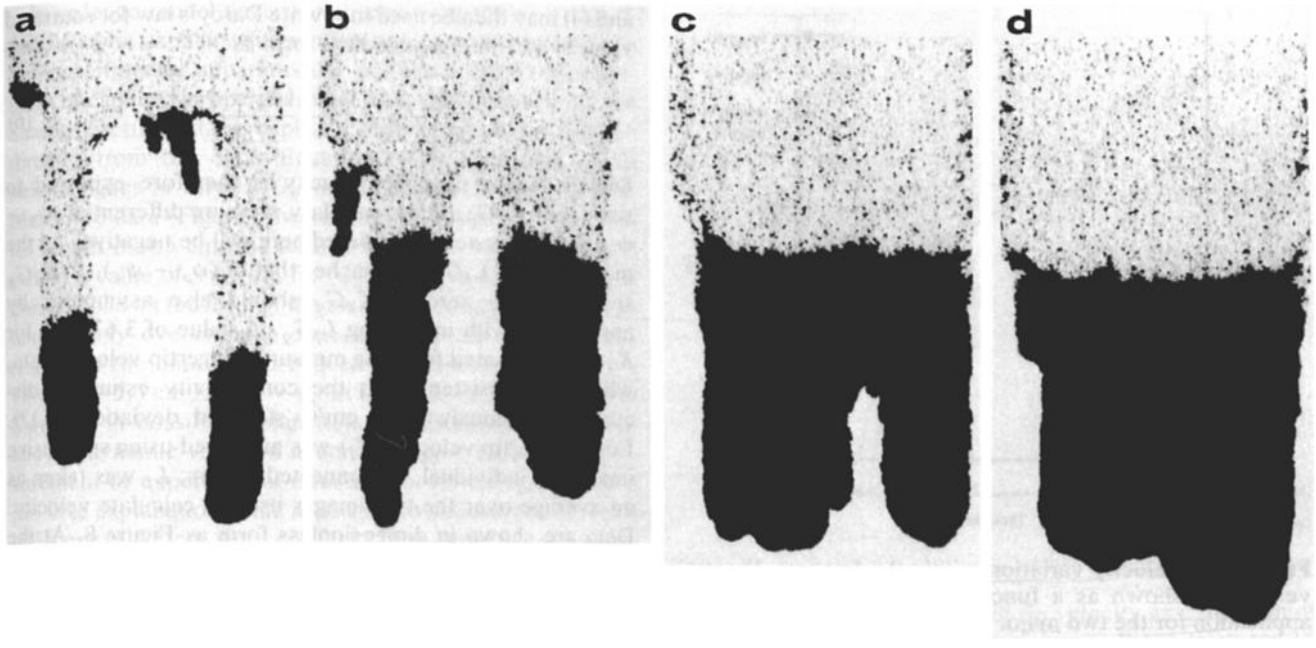

Figure 5. Effects of L_i on finger development (G_g for all images is 0.75): (a) experiment 8, L_i = 9.43 cm, t = 31 s; (b) experiment 10, L_i = 18.68 cm, t = 23 s; (c) experiment 11, L_i = 28.17 cm, t = 23 s; and (d) experiment 12, L_i = 33.47 cm, t = 23 s.

advancement shown, while the one shown in Figure 6d required only 23 s. As difference in L_i between the two experiments is minimal (9.08 cm versus 8.99 cm), the increase in velocity is attributed to the eightfold increase in G_g (0.125–1.00); again intermediate cases (Figures 6b and 6c) are consistent. Qualitative analysis suggests that while both are positively correlated to finger velocity, G_g has a higher-order effect than L_i does.

For quantitative analysis, fingertip velocity was defined as the rate of change in position of the leading edge of the tip, measured parallel to G_g. At a given G_g, fingertip velocity is expected to be a function of the capillary gradient acting within the tip. As the fingertip advances, the small-scale heterogeneity characteristic of all rough-walled fractures acts to continuously alter the shape of the wetting and drying fronts. This fluctuation in wetted structure causes dynamic variation in the capillary gradient. As previously stated, the advancing fingertip leaves behind a partially drained zone.

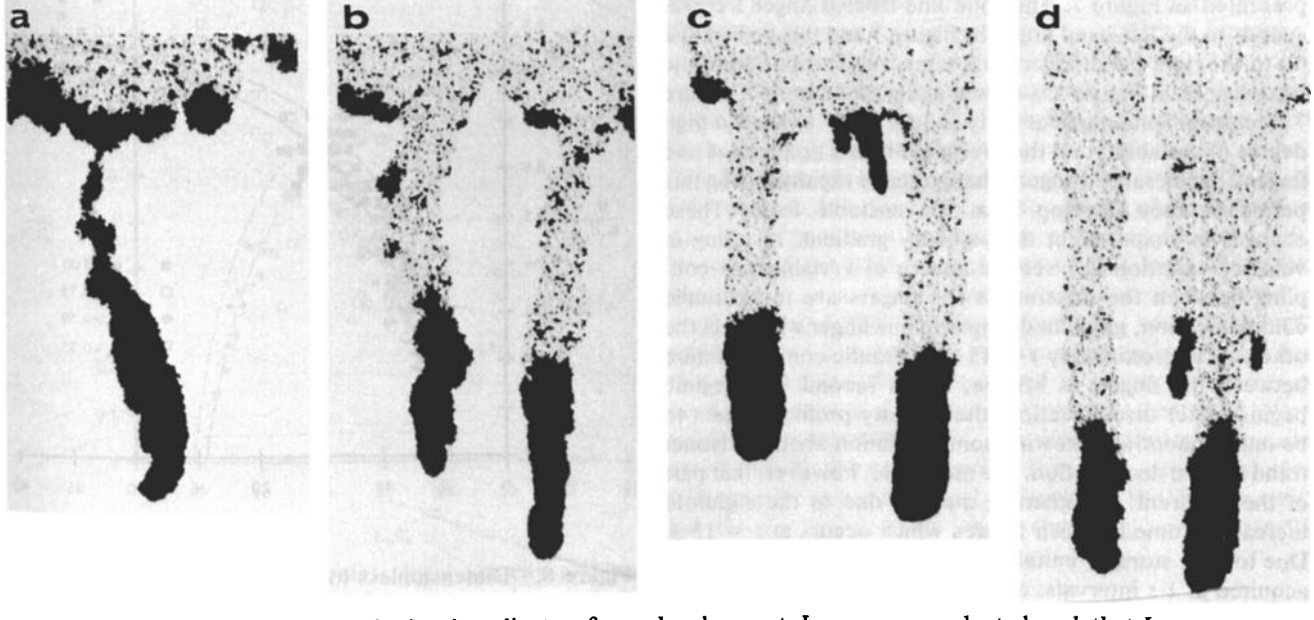

Figure 6. Effects of gravitational gradient on finger development. Images were selected such that L_i was of a similar magnitude. (a) Experiment 6, G_g = 0.25, L_i = 9.08 cm, and t = 1518 s. (b) Experiment 2, G_g = 0.50, L_i = 9.85 cm, and t = 104 s. (c) Experiment 8, G_g = 0.75, L_i = 9.43 cm, and t = 31 s. (d) Experiment 13, G_g = 1.00, L_i = 8.99 cm, and t = 23 s.

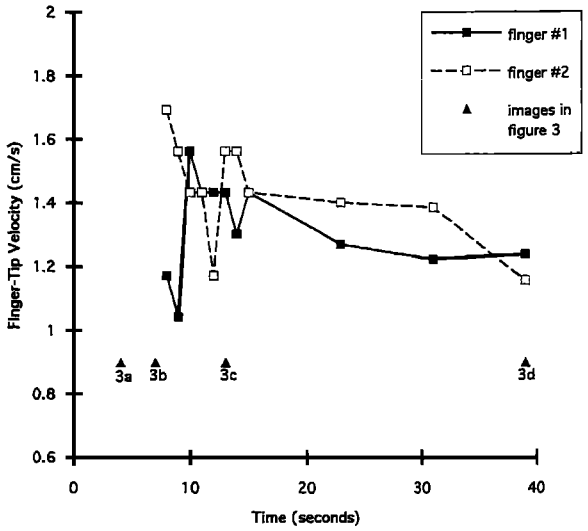

Figure 7. Velocity variation within the fracture. Fingertip velocity is shown as a function of time after initial fluid application for the two major fingers in experiment 8 (shown in Figure 3). Labeled markers illustrate when the images displayed in Figure 3 were acquired. Gradual trend toward deceleration is overlain by large local variation at early times. The two fingers remained in hydraulic communication until approximately $t = 15$ s.

This loss of fluid and consequent decrease in L_f is expected to slow the fingertip as it advances. Because the change of shape and loss of fluid are coupled dynamic processes, actual behavior is quite complex. A sudden narrowing and lengthening of the fingertip may lead to a local increase in tip velocity.

Both deceleration and local tip velocity fluctuations are readily apparent in plots of fingertip velocity in time. As an illustrative example, small-scale velocity measurements collected from the two significant fingers shown in Figure 3 are presented as Figure 7. The solid line labeled finger 1 corresponds to the left-hand finger in Figure 3 and the dashed line (2) to the right-hand finger. The temporal distribution of the images seen in Figure 3 is shown along the bottom of Figure 7. Measurements made at early time ($t < 15$ s) show a high degree of variability; on the average, finger 1 accelerates and finger 2 decelerates. Fingers change shape rapidly during this period as they develop from the unstable front. These changes in shape affect the capillary gradient, resulting in velocity variations. A second source of variability is coupling between the fingers. As the fingers are in hydraulic communication, gradient changes in one finger will affect the other. At approximately $t = 15$ s, hydraulic communication between the fingers is broken, and a second flow regime begins. After disconnection, the velocity profile appears to be much smoother, showing some variation about a distinct trend toward deceleration. We must note, however, that part of the apparent smoothening may be due to the eightfold increase in time between images which occurs at $t = 15$ s. Due to data storage limitations, only the first 16 images are acquired at 1-s intervals; at later times data are acquired at longer intervals, in this case 8 s.

If air and water entry pressure heads are assumed to be independent of velocity, (4) implies that G_c within a disconnected fingertip will be solely a function of L_f. Equations (3) and (4) may then be used to rewrite Darcy's law for saturated velocity (V) in dimensionless form as

$$\frac{V}{K_s G_g} = -\left\{1 + \frac{(\psi_a - \psi_w)}{L_f G_g}\right\} \tag{6}$$

Dimensionless fingertip velocity is therefore expected to scale with $L_f G_g$. Static capillary pressure differential ($\psi_a - \psi_w$) for the system considered here will be negative. As the magnitude of $L_f G_g$ approaches that of ($\psi_a - \psi_w$), $V/K_s G_g$ should go to zero; $V/K_s G_g$ should also asymptotically approach 1 with increasing $L_f G_g$. A value of 3.67 cm/s for K_s was estimated from the measured fingertip velocity data, which is consistent with the conductivity estimates discussed previously (3.48 cm/s; standard deviation, 0.12). Local fingertip velocity (V_l) was measured using successive images of individual, disconnected fingers; L_f was taken as an average over the two images used to calculate velocity. Data are shown in dimensionless form as Figure 8. At the lowest G_g explored (0.25), the analog fracture was of insufficient length for individual fingers to disconnect and stabilize. As a result, some measurements were taken prior to disconnection; these are reported for completeness but may be less reliable than those collected at larger G_g (0.5, 0.75, 1.00). At large dimensionless velocities (>0.5), the shape of the fingertips, and hence capillary gradient, changes rapidly with respect to the measurement interval (typically 1 s). The resultant measurement fluctuations are believed to be responsible for the increased data scatter observed as the limiting velocity is approached. Local fluctuation may be reduced by averaging the data to obtain single values of fingertip velocity (V_{la}) and fingertip length (L_{fa}) for each finger measured. Averaged data (Figure 9) show a significant reduction in data scatter, further emphasizing the apparent functional relationship.

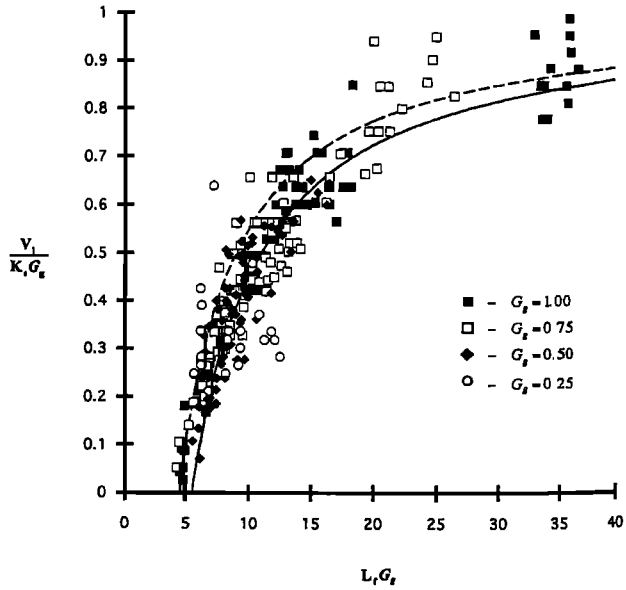

Figure 8. Dimensionless local velocity and tip length. $V_l/K_s G_g$ provides a measure of small-scale velocity relative to gravity-driven saturated flux, and the $L_f G_g$ provides a measure of the capillary forces opposing flow. The dashed and solid curves reflect (6) for values for $\psi_a - \psi_w$ of -4.5 and -5.5 cm, respectively.

In order to model fingertip velocity using (6), an estimate for the static capillary differential ($\psi_a - \psi_w$) is required. As the experimental apparatus did not allow direct measurement of capillary properties away from the boundaries of the analog fracture, static capillary differential was estimated directly from the data. Equation (6) implies that as tip velocity goes to zero, $L_f G_g$ should approach $-(\psi_a - \psi_w)$. Measured data (Figure 8) were used to estimate a minimum tip length of 4.5 cm; the dashed curves in Figures 8 and 9 reflect a value of −4.5 cm for ($\psi_a - \psi_w$) in (6). This model closely follows the form of the measured data, but appears to consistently overestimate dimensionless velocity. A superior fit to the data was produced by arbitrarily selecting a value of −5.5 cm for $\psi_a - \psi_w$ in (6) (solid curves in Figures 8 and 9). A possible explanation for this apparent discrepancy is dynamic variation in contact angle. However, measurement or experimental error cannot be disregarded as a possible explanation. Data appearing to indicate a horizontal intercept at 4.5 cm were collected from three exceptionally narrow fingers in two separate experiments. It is possible that these fingers did not fully sample the aperture field and are hence not representative. Additionally, due to the rounded nature of the wetting front and structural complication of the drying front, measured L_f is likely to overestimate the average fingertip length. At the conclusion of each experiment, the fluid column restrained from drainage by air entry pressure was measured, along with capillary rise. These measurements showed significant variation with respect to both L_i and G_g, implying that the experimental procedure did not allow the system to reach equilibrium prior to measurement. While these measurements are of questionable validity, they did imply a static capillary differential between −2.5 and −3.5 cm, significantly smaller than discussed above. Again, such variation would be consistent with dynamic variation in contact angle or may simply result from the combined effects of measurement errors and boundary effects.

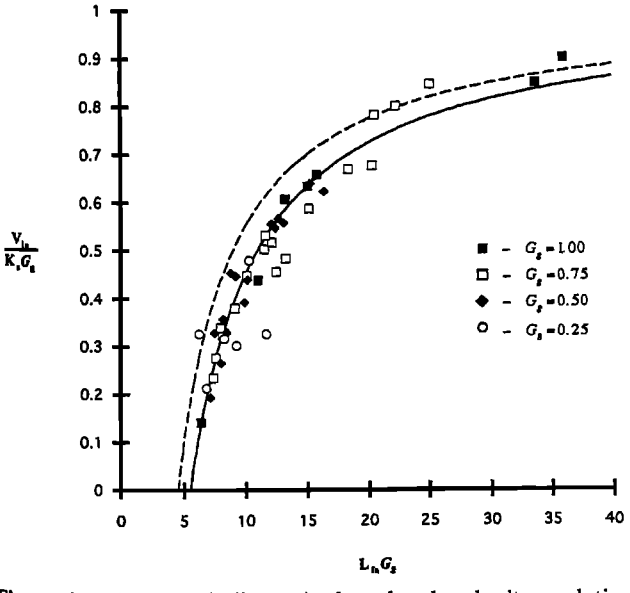

Figure 9. Averaged dimensionless local velocity and tip length. The data shown in Figure 8 are averaged to produce a single point for each individual finger, thereby reducing the effects of local fluctuation. The dashed and solid curves reflect (6) for values for $\psi_a - \psi_w$ of −4.5 and −5.5 cm, respectively.

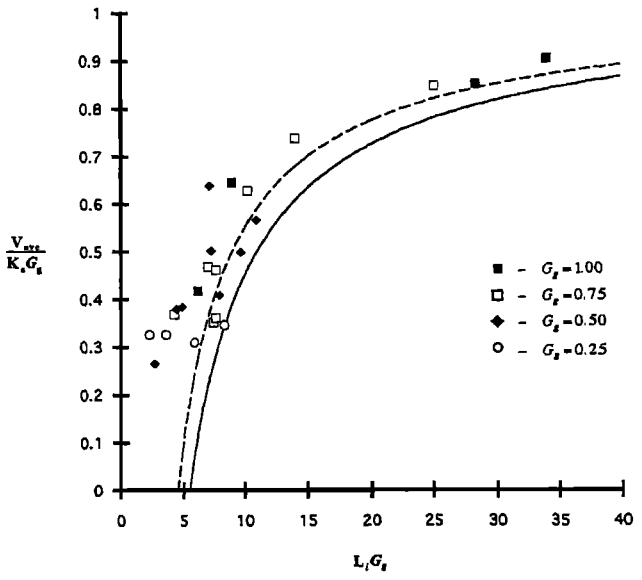

Figure 10. Experimental scale tip velocity as a function of scaled input. The data shown in Figure 9 are averaged to produce a single point for each experiment (V_{ave}). L_i provides a first-order approximation of average initial fingertip length. The dashed and solid lines reflect (6) for values for $\psi_a - \psi_w$ of −4.5 and −5.5 cm, respectively.

The functional relationship displayed by L_f and V_l is of limited predictive utility; L_f is a dynamic variable that is unknown a priori and V_l is associated with an individual finger. Therefore we explore the relationship between fluid input (L_i) and fingertip velocity at the experimental scale. Measurements presented in Figure 9 are averaged by experiment to produce an experimental scale average fingertip velocity (V_{ave}), which describes the significant disconnected fingers in each experiment (Table 1). From the results presented above, V_{ave} is expected to exhibit a functional relationship with $L_i G_g$. As is shown in Figure 10, data appear shifted to the left of (6), implying that L_i consistently underestimates average L_f. Instability concentrates fluid from the distributed front into individual fingers; hence initial tip length may be greater than the initial depth of infiltration as described by L_i. The amount of concentration will be a function of the number of fingers, finger width, structure of the front, and amount of fluid lost wetting the fracture. As a result, experimental scale data are expected to display a less distinct functional form than seen at the local scale (Figures 8 and 9). Simple theory (equation (5)) implies that some minimum L_f is required to initiate finger movement. However, if a distributed front is concentrated into a single finger, the minimum L_i required to initiate movement may be small; the data shown in Figure 10 are inconclusive with respect to a minimum L_i. Similarly, the data suggest, but do not conclusively show that V_{ave} asymptotically approaches saturated conductivity.

Finger Width

On a qualitative basis, it appears that increasing L_i leads to increased finger width (Figure 5); conversely, increasing G_g has an apparently indeterminate effect on finger width

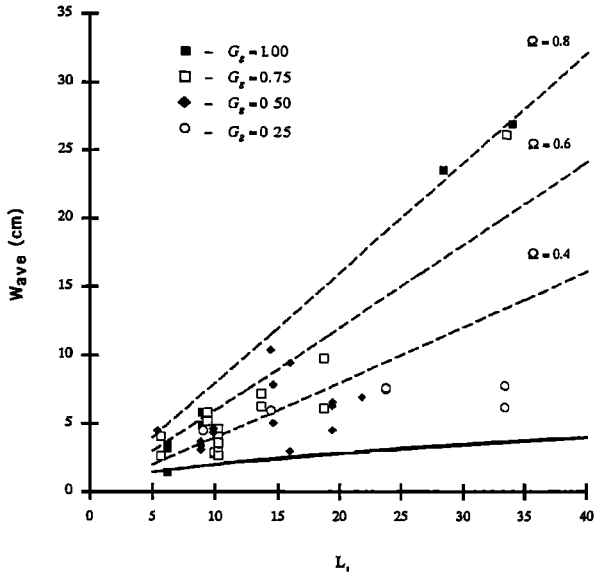

Figure 11. Experimental average finger width shown as a function of L_i. W_{ave} is seen to increase with L_i. The data taken at various gradients are intermixed, suggesting that the effects of G_g are of a lower order than other factors, such as the amplitude of the initial perturbation at the onset of instability. The solid line reflects (8) for Hele-Shaw cells and the dashed lines reflects (9) for three-dimensional porous media.

(Figure 6). For quantitative analysis, finger width was defined as the average width of the wetted domain, measured normal to G_g over a region free from boundary effects. As was done for fingertip velocity, measurements were taken from significant fingers which were disconnected from adjacent fingers; W_{ave} was defined as the experimental average width of measured fingers in a given experiment. The data (Figure 11 and Table 1) confirm qualitative observations; W_{ave} increases with L_i and shows no consistent relationship with G_g.

Linear stability theory predicts the growth of a dominant wavelength that may serve as a estimator of finger width [*Saffman and Taylor*, 1958; *Chouke et al.*, 1959; *Glass et al.*, 1991]. Linear analysis requires the velocity of an equivalent unperturbed front; this should be given by the velocity of the front at the onset of instability ((6) with L_i substituted for L_f). Finger width (W) for displacement of air by water may then be written for Hele-Shaw cells as [after *Chouke et al.*, 1959]

$$W = \pi\sqrt{3}\left[\frac{\sigma L_i}{-\rho g(\psi_a - \psi_w)}\right]^{1/2} \tag{7}$$

where σ is surface tension at the air-water interface. The solid line in Figure 11 reflects (7) assuming standard properties of water at 25°C and that $\psi_a - \psi_w = -5.5$ cm. It appears from the data that the Hele-Shaw model, which describes a smooth-walled fracture, provides an approximate lower bound on finger width in the rough-walled analog fracture. However, several fingers were observed to be somewhat narrower than given by (7). For three-dimensional porous media, linear analysis gives finger width as [after *Glass et al.*, 1991]

$$W = \frac{2\pi\Gamma}{K_s(\psi_a - \psi_w)} L_i \tag{8}$$

where Γ is a function of the initial moisture content and sorptivity in the local vicinity of the advancing tip. As these quantities are unknown, the first term on the right-hand side of (8) is treated as a lumped parameter (Ω) and displayed as a family of curves (dashed lines) in Figure 11; values were arbitrarily selected such that the resultant lines would pass through the measured data (Ω = 0.4, 0.6, and 0.8). The uppermost line appears to bound measured behavior and may be the most appropriate. Both (7) and (8) are independent of G_g, which is consistent with experimental observations.

Linear theory is based on an assumption of initially infinitesimal perturbations that remain small, and therefore may be inappropriate for the finite amplitude disturbances considered in these experiments. Experimental observations suggest that finger width is of the same order as that of the associated perturbation at the onset of instability, i.e., approximately one half the perturbation wavelength. Consider the behavior of an idealized finite amplitude sinusoidal front of wavelength λ_a during the transition to instability. Due to the sinusoidal nature of the front, approximately half of the front will have an L_f greater than average, while for the rest of the front L_f will be smaller than average. Therefore from (3) and (4) one would expect then that the regions of higher gradient (smaller L_f) would advance, forming fingers of width $\lambda_a/2$. While the entire front is in hydraulic communication, fluid is freely available to the advancing tip and no narrowing of the finger is expected. After fingers separate from each other, fingertips will lose fluid during advancement, causing a shortening and narrowing of the fingertip as seen in Figures 6b, 6c, and 6d. The finger shown in Figure 6a did not disconnect from the fluid source, and hence did not experience the tip narrowing associated with fluid loss.

Observed correlation between finger width and L_i is believed to be related to damping of initial perturbations, as discussed briefly in a previous section. The fluid application process initially introduces a characteristic perturbation wavelength of approximately 1.6 cm due to the syringe spacing. As imbibition proceeds, damping stretches this initial wavelength. The amount of damping appears to be related to the distance traveled as a stable front, which will increase with L_i. Therefore finger width should also increase with L_i, a result consistent with experimental observations (Figure 11). Due to damping during imbibition, one half the initial perturbation wavelength ($\lambda_a/2 \sim 0.8$ cm) should provide an estimate of the minimum finger width expected. Experimental results were consistent with this approximation; the smallest finger width observed was 1.028 cm (experiment 25). In natural systems, finite amplitude disturbances are expected to be the rule rather than the exception; therefore prediction of finger width will require an understanding of both the mechanisms responsible for inducing perturbations and subsequent damping during stable infiltration.

Hypothetical Field Scenario

To illustrate the potential implications of gravity-driven instability, we propose a hypothetical scenario where spa-

tially extensive, nonhorizontal fractures similar to the analog fracture used in this study dissect an initially dry, low-permeability rock unit and are exposed at the surface. A sudden rainfall event over such terrain would likely result in surface ponding, creating a boundary condition analogous to the slug input boundary considered in the experiments presented here. For illustrative purposes we assume that each meter of fracture length is supplied by a square meter of run-off area, and that fluid transfer to the fracture is loss-free. Under such conditions, a very small rainfall event of 0.001–0.0085 cm would produce applied fluid depths (L_i) of about 5–40 cm. Local heterogeneity along the surface exposure would create point connections into the fracture, resulting in perturbations to the front analogous to those induced by our experimental procedure. Small infiltration events, such as that considered here, would become unstable a short distance into the fracture (~5–40 cm). The resultant fingers would probably then advance an additional ~1–10 m along the fracture before the fingertips would freeze in place. The short-term wetted structure would be moistened to field capacity of the fracture and resemble a comb, consisting of a backbone along the surface and fingers extending downgradient, ending in the fingertips. By analogy to porous media studies [*Glass et al.*, 1989c], such a wetted structure may provide preferred flow paths for subsequent infiltration events.

Conclusions

Using a natural fracture sample, we have established that gravity-driven instability can occur in nonhorizontal, unsaturated fractures and is a separate process from heterogeneity-induced channeling. To explore gravity-driven instability, a systematic experimental approach was developed using a transparent analog rough-walled fracture. Under dry initial conditions, gravity-driven instability was shown to result from three different boundary conditions: redistribution of flow at the cessation of a stable infiltration event, inversion of a stable, density-stratified system (air overlying water), and infiltration flow at less than the gravity-driven saturated flux ($K_s G_g$).

The redistribution of flow at the cessation of stable infiltration was explored through systematic experimentation using a slug input boundary condition into the analog fracture under initially dry conditions. Parameters varied were limited to gravitational gradient (G_g) and depth of fluid applied (L_i). Measurements were made of fingertip velocity, fingertip length, and finger width. Tip velocity exhibited local variation that was most pronounced during the period after redistribution when adjacent fingers remain in hydraulic communication. Fingers were also observed to exhibit a general trend toward deceleration. Advancing fingers lose fluid by wetting the fracture, thereby increasing the capillary gradient opposing flow which causes the finger to slow and eventually stop. A functional relationship was established between dimensionless fingertip velocity and length of the connected fluid column comprising the fingertip; the nature of this relationship underscores the importance of capillary gradient with respect to finger behavior. At the experimental scale, the depth of fluid applied to the fracture (L_i) displays a functional relationship with average fingertip velocity similar in form to that seen at the local scale. However, as instability concentrates the infiltrating fluid into fingers, L_i consistently underestimates average fingertip length.

The structure of the wetting front at the onset of instability appears to have a significant effect on development of fingers. The number of fingers formed and their spatial distribution exhibited strong correlation with the distribution and magnitude of finite amplitude perturbations to the wetting front at the onset of instability. At first order, finger width appears to be a function of perturbation size at the onset of instability. The influence of L_i is apparently limited to damping of the initial perturbations during the initial, stable infiltration phase, while gravitational gradient does not appear to affect finger width to any significant degree. Linear stability theory derived for smooth-walled Hele-Shaw cells may provide a lower bound on finger width.

Future Research

The transient boundary condition used in these experiments did not allow measurement of flux through the system. Implementation of a constant flux boundary condition is expected to stabilize finger velocity and allow systematic variation of flux through an individual finger. It is expected that such experimentation will lead to the development of higher-order relationships for finger velocity and provide an improved understanding of finger width as a function of system parameters.

Existing linear stability theory for fluid-fluid displacement was developed on the basis of infinitesimal perturbations (see reviews by *Saffman* [1986] and *Homsy* [1987]). While the mechanism for instability is independent of perturbation amplitude, predictive models for finger width assuming growth from infinitesimal perturbations are not expected to be appropriate for fingers initiated from finite amplitude perturbations. In the experiments presented here, finite amplitude perturbations to the front at the onset of instability apparently dominated subsequent behavior; measured finger width was inconsistent with predictions based on linear stability theory for both porous media and Hele-Shaw cells. The stability of individual viscous fingers to finite amplitude perturbations has been considered by several researchers (see review by *Bensimon et al.* [1986]); however, we are currently unaware of any research which directly considers the effects of finite amplitude perturbations on gravity-driven instability. In a natural fracture system, finite amplitude perturbations will result from both local heterogeneity and preferential flow; therefore it is necessary to explicitly consider the effects of perturbation size on wetting front instability.

During slow imbibition into a horizontal fracture, flow is expected to preferentially follow paths of connected small apertures within the fracture. This heterogeneity-induced channeling is expected to dominate formation of the wetted structure for times short with respect to matric effects. Inclination of the fracture introduces gravitational forces. Hence wetted structure is expected to result from the coupled effects of gravity-driven instability and heterogeneity-induced channeling. As inclination increases, the effects of gravity will become increasingly significant. In homogeneous systems such as the analog fracture used here, the path of individual fingers will show little deviation from the downgradient direction. However, in highly heterogeneous fractures, channeling through low-permeability zones may always dominate. The problem of heterogeneity (and anisotropy) may be approached experimentally both through use of analog fractures of controlled spatial properties and epoxy casts of natural fractures. As it is not realistic to produce all

possible heterogeneous structures in the laboratory, pore scale modeling techniques such as the modified invasion percolation model developed by *Glass* [1993a, b] will be necessary to fully explore coupling between the two flow processes.

The effects of initial moisture content on gravity-driven instability must also be considered. In porous media, fingers have been observed to exhibit spatial persistence; passage of an unstable front creates preferred flow paths for subsequent events [*Glass et al.*, 1989c]. Such behavior is extremely important in terms of modeling contaminant transport, as it causes subsequent infiltration events to penetrate the system rapidly. Also important is behavior within a partially saturated, uniform initial moisture field. Experiments in porous media suggest that the occurrence of wetting front instability in uniform moisture fields is a function of the initial moisture content [*Diment and Watson*, 1985].

Acknowledgments. The authors gratefully acknowledge the assistance and support provided by the following: W. C. Ginn in design and fabrication of the experimental apparatus, L. Orear in development of image acquisition software, H. A. Nguyen in experimentation, and P. B. Davies, D. L. Norton, and S. R. Sobolik for their careful and constructive reviews. This work was supported by the U.S. Department of Energy, Office of Civilian Radioactive Waste Management, Yucca Mountain Site Characterization Project Office, under contract DE-AC04-76DP00789. The first author was supported for a portion of this work by the George Burke Maxey Hydrology/Hydrogeology Fellowship, donated by Mrs. Elizabeth Stout and administered by the Desert Research Institute, University of Nevada System.

References

Bensimon, D., L. P. Kadanoff, S. Liang, B. I. Shraiman, and C. Tang, Viscous flows in two dimensions, *Rev. Mod. Phys.*, *58*(4), 977–999, 1986.

Bourke, P. J., E. M. Durrance, M. J. Heath, and D. P. Hodgkinson, Fracture hydrology relevant to radionuclide transport—Field work in a granite formation in Cornwall, report, Comm. of the Eur. Communities, Luxembourg, 1985.

Chouke, R. L., P. van Meurs, and C. van der Poel, The instability of slow immiscible, viscous liquid-liquid displacements in porous media, *Trans. Am. Inst. Min. Metall. Pet. Eng.*, *216*(8073), 1959.

de Gennes, P. G., Imperfect Hele-Shaw cells, *J. Phys. Lett.*, *47*(9), 1541–1546, 1986.

Diment, G. A., and K. K. Watson, Stability analysis of water movement in unsaturated porous materials, 3, Experimental studies, *Water Resour. Res.*, *21*, 979–984, 1985.

Eaton, R. R., N. E. Bixler, and R. J. Glass, Predicting flow through low-permeability, partially saturated, fractured rock—A review of modeling and experimental efforts at Yucca Mountain, in *Selected Papers on Hydrogeology From the 28th International Geological Congress*, vol. 2, *Hydrogeology of Low Permeability Environments*, edited by S. P. Neuman and I. Neretnieks, pp. 239–268, Verlag Heinz Heise, Hannover, Germany, 1990.

Evans, D. D., and T. J. Nicholson, Flow and transport through unsaturated rock: An overview, in *Flow and Transport Through Unsaturated Fractured Rock, Geophys. Monogr. Ser.*, vol. 42, edited by D. D. Evans and T. J. Nicholson, pp. 1–10, AGU, Washington, D. C., 1987.

Glass, R. J., Modeling gravity-driven fingering using modified percolation theory, paper presented at the Fourth Annual International Conference on High Level Radioactive Waste Conference, Am. Soc. Civ. Eng./Am. Nucl. Soc., Las Vegas, Nev., April 26–30, 1993a.

Glass, R. J., Gravity-driven fingering in rough-walled fractures: Analysis using modified percolation theory, *Eos Trans. AGU*, *74*(16), Spring Meeting suppl., 149, 1993b.

Glass, R. J., and V. C. Tidwell, Research program to develop and validate conceptual models for flow and transport through unsaturated, fractured rock, paper presented at the Second Annual International Conference on High Level Radioactive Waste Management, Am. Soc. Civ. Eng./Am. Nucl. Soc., April 28 to May 3, Las Vegas, Nev., 1991.

Glass, R. J., T. S. Steenhuis, and J.-Y. Parlange, Wetting front instability as a rapid and far-reaching hydrologic process in the vadose zone, *J. Contam. Hydrol.*, *3*, 207–226, 1988.

Glass, R. J., J.-Y. Parlange, and T. S. Steenhuis, Wetting front instability, 1, Theoretical discussion and dimensional analysis, *Water Resour. Res.*, *25*, 1187–1194, 1989a.

Glass, R. J., T. S. Steenhuis, and J.-Y. Parlange, Wetting front instability, 2, Experimental determination of relationships between system parameters and two-dimensional unstable flow field behavior in initially dry porous media, *Water Resour. Res.*, *25*, 1195–1207, 1989b.

Glass, R. J., T. S. Steenhuis, and J.-Y. Parlange, Mechanism for finger persistence in homogeneous unsaturated porous media: Theory and verification, *Soil Sci.*, *148*, 60–70, 1989c.

Glass, R. J., J.-Y. Parlange, and T. S. Steenhuis, Immiscible displacement in porous media: Stability analysis of three-dimensional, axisymmetric disturbances with application to gravity-driven wetting front instability, *Water Resour. Res.*, *27*, 1947–1956, 1991.

Hakami, E., Water flow in single rock joints, *SKB Tech. Rep. 89-08*, Swed. Nucl. Fuel and Waste Manage. Co., Stockholm, 1989.

Hill, D. E., and J.-Y. Parlange, Wetting front instability in layered soils, *Soil Sci. Soc. Am. Proc.*, *36*, 697–702, 1972.

Homsy, G. M., Viscous fingering in porous media, *Annu. Rev. Fluid Mech.*, *19*, 271–311, 1987.

Maxworthy, T., The nonlinear growth of a gravitationally unstable interface in a Hele-Shaw cell, *J. Fluid Mech.*, *177*, 207–232, 1987.

Neretnieks, I., T. Eriksen, and P. Tahtinen, Tracer movement in a single fissure in granitic rock: Some experimental results and Their interpretation, *Water Resour. Res.*, *18*, 849–858, 1982.

Neretnieks, I., Solute transport in fractured rock—Applications to radionuclide waste repositories, *SKB Tech. Rep. 90-38*, Swed. Nucl. Fuel and Waste Manage. Co., Stockholm, 1990.

Nicholl, M. J., R. J. Glass, and H. A. Nguyen, Gravity-driven fingering in unsaturated fractures, paper presented at the Third Annual International Conference on High Level Radioactive Waste Conference, Am. Soc. Civ. Eng./Am. Nucl. Soc., Las Vegas, Nev., April 12–16, 1992.

Pruess, K., and J. S. Y. Wang, Numerical modeling of isothermal and nonisothermal flow in unsaturated fractured rock—A review, in *Flow and Transport Through Unsaturated Fractured Rock, Geophys. Monogr. Ser.*, vol. 42, edited by D. D. Evans and T. J. Nicholson, pp. 11–21, AGU, Washington, D. C., 1987.

Saffman, P. G., and G. Taylor, The penetration of a fluid into a porous medium or Hele-Shaw cell containing a more viscous liquid, *Proc. R. Soc. London A*, *245*, 312–331, 1958.

Saffman, P. G., Viscous fingering in Hele-Shaw cells, *J. Fluid Mech.*, *173*(73), 73–94, 1986.

Snow, D. T., The frequency and apertures of fractures in rock, *Int. J. Rock Mech. Min. Sci.*, *7*, 23–40, 1970.

White, I., P. M. Colombera, and J. R. Philip, Experimental study of wetting front instability induced by sudden change of pressure, *Soil Sci. Soc. Am. J.*, *40*, 824–829, 1976a.

White, I., P. M. Colombera, and J. R. Philip, Experimental study of wetting front instability induced by gradual change of pressure gradient and by heterogeneous porous media, *Soil Sci. Soc. Am. J.*, *41*, 483–489, 1976b.

R. J. Glass and M. J. Nicholl, Geoscience Center, Department 6115, Sandia National Laboratory, Albuquerque, NM 87185.

S. W. Wheatcraft, Department of Geological Sciences, University of Nevada, Reno, NV 89557.

(Received June 24, 1993; revised January 10, 1994; accepted January 17, 1994.)